Journal of Magnetic Resonance **146,** 223–227 (2000)
doi:10.1006/jmre.2000.2130, available online at http://www.idealibrary.com on IDEAL®

Single-Coil Surface Imaging Using a Radiofrequency Field Gradient

Nathalie Baril, Eric Thiaudière, Bruno Quesson, Christophe Delalande, Paul Canioni, and Jean-Michel Franconi[1]

Unité de Résonance Magnétique des Systèmes Biologiques, UMR 5536 CNRS-Université Victor Segalen Bordeaux 2, 146 rue Léo Saignat, 33076 Bordeaux Cedex, France

E-mail: jmichel.franconi@rmsb.u-bordeaux2.fr

Received March 13, 2000; revised May 22, 2000

A method for in-plane imaging of large objects as compared to the RF coil is proposed based on the use of a single specially designed surface coil, without using B_0 gradients. A constant B_1 gradient was generated along the main axis of a ladder-shaped coil, and RF-encoding along the direction of the gradient made it possible to obtain spin–density profiles. Successive acquisitions of profiles obtained by translation of the NMR coil resulted in distorted images—due to the presence of non-zero gradients perpendicular to the constant gradient—that were successfully processed using a mathematical treatment based on linear combinations of calculated altered images from single-pixel objects.

NMR imaging using radiofrequency field gradients, first introduced by Hoult (*1*), is an interesting alternative to conventional MRI based on static magnetic field gradients. Two main applications of the use of B_1 gradients have been developed (for review, see (*2*)), NMR microscopy and diffusion measurements. The former was possible thanks to large B_1 gradients generated by a loop much larger than the imaged object. This method proved to be fast and efficient for 1D imaging (*3–6*). A complete 2D imaging was achieved by rotating the object and by processing the data as a whole (*7, 8*). On an other hand, diffusion-controlled motions were encoded by two successive B_1 pulses spaced with increasing delays (*9–11*); artifacts of the method and remedies were reported by Humbert *et al.* (*12*). However, in both applications, the described pulse sequences required at least one RF pulse generating a defined nutation angle, and thus the use of an additional homogeneous B_1 coil.

In this study, a method for in-plane NMR imaging is proposed, with a dedicated NMR coil generating a linear and constant B_1 gradient over a large distance. Such a gradient made it possible to encode one dimension and obtain spin–density profiles. Two-dimensional images were obtained by moving the coil across the other direction. A nonnegligible B_1 gradient in this direction induced distortions which were analyzed and corrected by a simple numerical procedure.

[1] To whom correspondence should be addressed.

DESIGN OF THE RF COIL: THE LADDER-SHAPED COIL

The selected geometry to obtain a B_1 gradient uniform over the largest possible volume had a shape of a ladder with a defined wiring (rungs). First, a rectangular (5 cm times 2.5 cm) loop was made with a copper wire which was extended so as to draw additional loops (10 cm, 15 cm, and 20 cm in length). The four loops were superimposed so that the sides of the ladder exhibited a variable number (from 1 to 4 as a function of the z-axis) of conducting copper wires along the main axis (so-called "ladder-shaped coil," Fig. 1). The increase in current created in this way in the circuit was expected to generate the radiofrequency field gradient.

The ladder-shaped coil was then considered as a sum of individual line segments for which the Biot–Savart differential equation was analytically solved. The B_1 vectors for every segment were then added to each other in order to calculate the B_1 modulus generated by the whole coil. Figures 2A and 2B show the contour plots of the calculated radiofrequency field generated by the ladder-shaped coil in the yz plane and the xy plane, respectively. The B_1 variations along the z and x axes are also illustrated (Figs. 2C and 2D). To check the effective magnetic field distribution of the ladder-shaped coil, B_1-mapping was carried out using the well-described sequence MISSTEC associating a spin echo (SE) and a stimulated echo (STE) (*13*). The measured moduli of B_1 in the (y, z) and the (x, y) planes are given in Figs. 3A and 3B. Due to experimental uncertainty for small nutation angles (i.e., less than 40°), only a range of values is displayed. The B_1 values along the z axis and the field profile along the x axis are given in Figs. 3C and 3D, respectively. The B_1 gradient values were typically 70 μT/m in the z-direction at $x = 0$ and $y = 3$ cm whereas values of only 40 μT/m were obtained at $x = \pm 2$ cm.

IMAGING IN THE ROTATING FRAME AND IMAGE PROCESSING

PseudoFIDs (*14*) were acquired with the main axis of the coil parallel to z. Fourier transform of individual pseudoFID should give the spin–density profiles as a function of z. The 2D image in the (x, z) plane would then be created by shifting the

1090-7807/00 $35.00

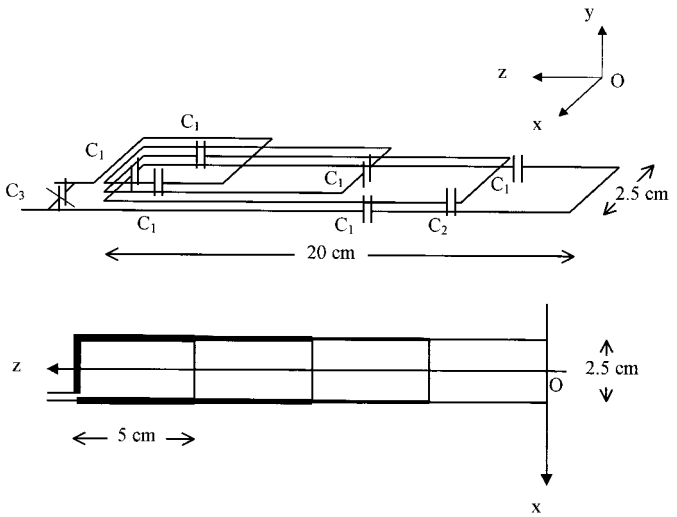

FIG. 1. Dimensions and orientation of the ladder-shaped coil in the (*x*, *y*, *z*) coordinates. The capacitors were inserted to tune it at the operating frequency, i.e., 200.3 MHz. Quality factor for the unloaded coil was 140.

coil across the *x* axis. Experiments were first attempted on a very simple water phantom (1 cm diameter, 2 cm length cylinder) placed at $z = 12$ cm and $y = -3$ cm. As the main axis of the cylinder was parallel to *y*, the shape of the imaged object in the *xz* plane was expected to be circular. Moreover, as the space resolution in the *x* axis was set to 1 cm (increment of the coil translation for successive acquisition of spin–density profiles), the phantom could be better considered as a point. The result is shown in Fig. 4A: magnetization that should be localized at the position (12, 7) appeared spread in a well-characterized pattern. The signal decreased and was visible at smaller positions of *z* as the coil was moved away from the *x*-position of the phantom.

Due to the presence of a non-zero gradient in the x direction, the coil placed at a given position x_0 is able to detect spin signals at a position $x_0 + \delta$. Because the B_1 amplitude at this position is smaller than in x_0, this signal is expected to be lower and shifted to smaller values for the *z*-coordinate after Fourier transformation. The signal received by the coil would depend

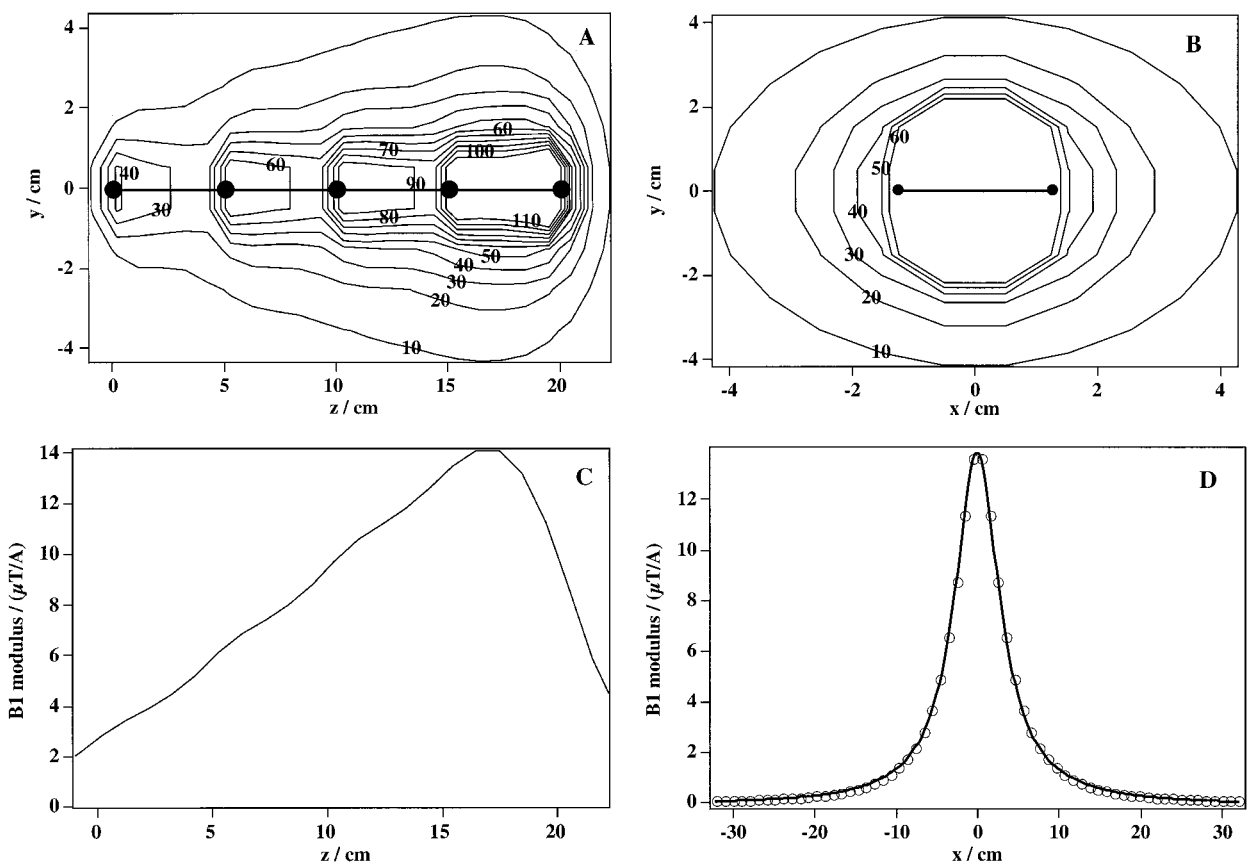

FIG. 2. Contour plots of the calculated radiofrequency field isointensity lines generated by the coil in μT for a current of 1 A, in the *yz* plane (A) and the *xy* plane at $z = 15$ cm (B). Modeling of the B_1 field was achieved using the Biot and Savart differential equation. The position of the coil is also displayed. (C) The B_1 gradient value along *z* (at $y = 4$ cm and $x = 0$ cm). This gradient is nearly constant over 15 cm. (D) The B_1 attenuation on the sides of the coil for $y = 4$ cm and $z = 15$ cm (circles). The curve could be reasonably fitted to a Lorentzian curve (continuous line), with a width at half height that was nearly constant along the *z* axis (not shown).

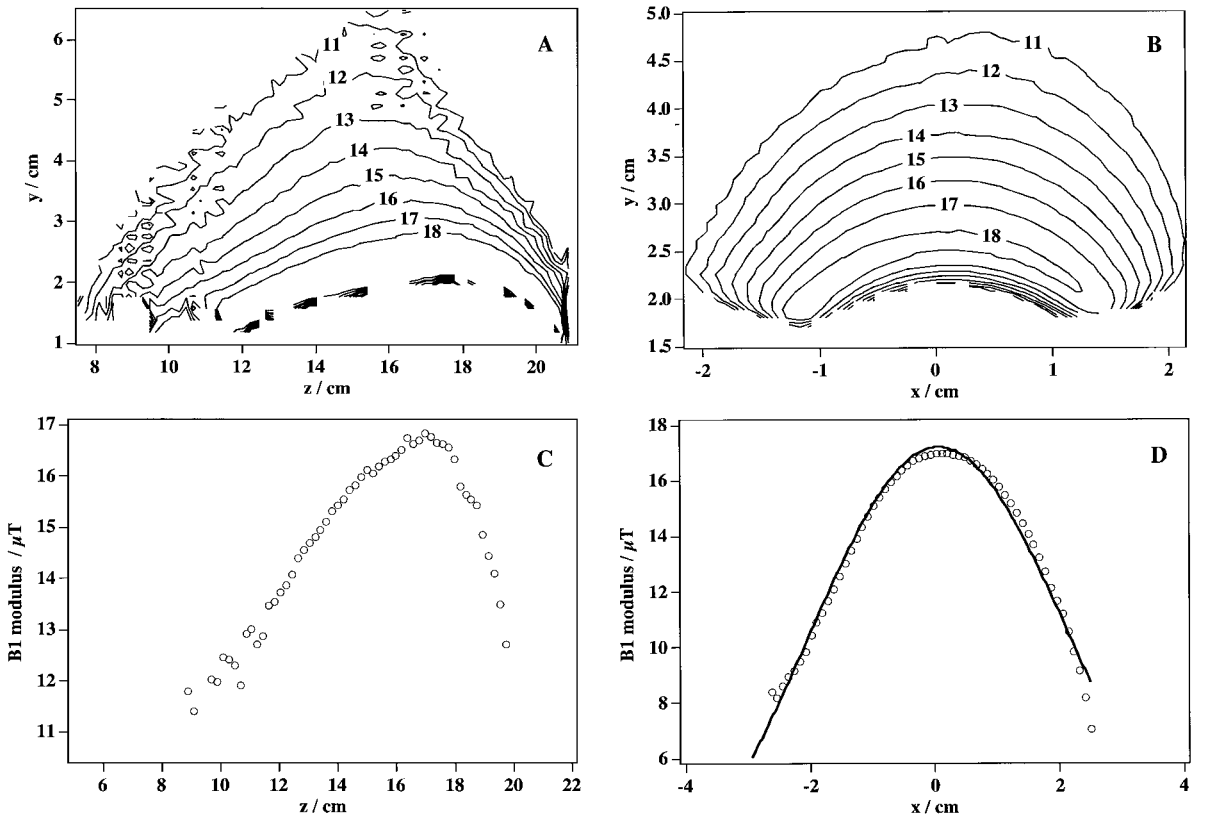

FIG. 3. Contour plots of the measured radiofrequency field isointensity lines generated by the ladder coil in μT, in the yz plane (A) and the yx plane (B). Under several experimental conditions, where the mixing time (30 ms) is very short as compared to T_1 (2.8 s),the STE/SE signal intensity ratio is equal to arcos(α) or arcos($\gamma \cdot B_1 \cdot T$p), where α is the nutation angle, γ the magnetogyric ratio, and Tp the rectangular pulse length. Experiments were carried out on a Bruker Biospec system equipped with a 50-cm bore magnet operating at 4.7 T (Bruker, Wissembourg, France). A 1.5 dm^3 parallelepipedic water phantom was placed close to the coil. Water shimming resulted in 20–30 Hz width at half height for the water resonance. (C) The B_1 gradient along z for $y = 3$ cm. A zone of quasi-linear variation of B_1 is observed, between $z = 9$ cm and $z = 17$ cm. (D) The B_1 field profile along the x axis for $y = 3$ cm and $z = 17$ cm (circles). The curve could be reasonably fitted to a Lorentzian curve as in Fig. 2D, but a slightly better fit was obtained using a Gaussian curve (continuous line).

on the magnetization M as follows, neglecting the relaxation processes,

$$S_{k_z, x_0, \delta} = \int_z \int_\delta \alpha(z) \cdot M_{z, x_0+\delta} \sin(k_z \cdot z \cdot g(\delta)) \cdot g(\delta) dz d\delta, \quad [1]$$

where k_z is the wave vector, namely, $\gamma \cdot G_1 \cdot T$p, with G_1 as the B_1 gradient along z at the position x_0, Tp as the pulse length, and $g(\delta)$ as the attenuation of B_1 as a function of δ. Here, $\alpha(z)$ is a factor that accounts for the coil receptivity, which is expected to increase linearly as a function of z because of the B_1 gradient. As mentioned previously, the $g(\delta)$ function is little dependent on z and will be assumed to depend only on δ. Therefore the Fourier transformation of S does not provide the true the magnetization map $M(z, x_0)$ but is affected by artifacts included in Eq. [1] (Fig. 4A). Distortions that would arise from B_1-encoding along the y-direction are neglected since only planar objects placed at a defined y-position are considered.

Let $M_{i,j}$ be the real magnetization distribution, i.e., the corrected image. The distorted image will be called $I_{k,l}$. In both cases, the first index is for rows (z-direction) and the second is for columns (x-direction). The dimensionality of M and I will be considered as equal. Then M and I will be represented as vectors, where the first index is incremented first. Each value at the position (z, x) in the vector $I_{k,l}$ may thus be considered as a linear combination of all the pixel intensities at the same position in distorted images from every possible position in the magnetization map $M_{i,j}$. Thus, $I_{k,l}$ might be written as

$$I_{k,l} = \text{“Distortion Matrix”} \times M_{i,j}. \quad [2]$$

Rows of the distortion matrix are arranged according to their kl index, while the columns are arranged according to the ij index. The size of the distortion matrix is thus (i times j) times (k times l). Each column indexed (i, j) contains a distorted image from a given pixel $M_{i,j}$. Reciprocally, each row indexed (k, l) shows how each position of $M_{i,j}$ contributes to a given pixel (k, l) of the distorted image. To build the distortion

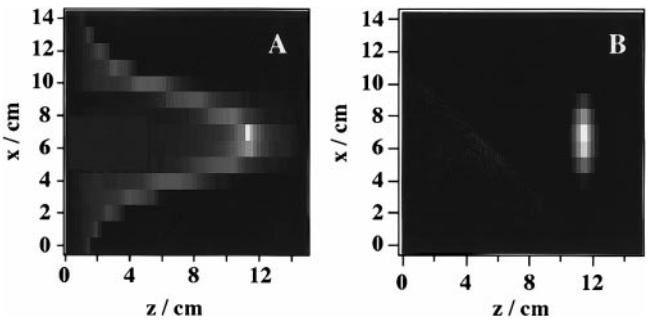

FIG. 4. (A) Distorted image from a very small water phantom placed at $z = 12$ cm, $x = 7$ cm, and $y = -2$ cm, after Fourier transformation of 15 pseudoFIDs acquired every 1 cm. Typical rectangular pulse length was 800 μs, $G_1 = 31$ μT/m, the delay between two consecutive pulses was 50 μs, and the number of pulses was 128. Such durations (that might appear quite long as compared to the observed T_2^*) were due to the apparatus limitations, especially for the RF amplifier duty cycle. Fourier transformation of pseudoFIDs resulted in density profiles made of 65 complex values. Clearly the image must be corrected in order to show where the spins really are. (B) Corrected image from Fig. 4A after the reconstruction protocol.

matrix, one way was to start from a distorted image from a small object considered as a point (Fig. 4A). The corresponding magnetization map was then considered as empty except for one pixel. The distorsion matrix could then be filled by acquiring the whole set of distorted images for every (x, z) position of the single-pixel object. Besides its heaviness (one distorted image should be recorded for each pixel position), this approach has two severe drawbacks. First, it introduces the experimental noise in the distorsion matrix. Second, additional experiments must be carried out if the image dimensionality changes, e.g., from (65, 15) to (128, 30). An alternative method is to start from a mathematical (noise-free) expression of the distorted image that takes into account the magnetization position as well as the decrease and the z-shift of the signal as a function of x. After a careful examination of several distorted images of the single-pixel object placed at different positions of z, it appeared that the signal decayed according to a Gaussian line as a function of x and was convolved by a Lorentzian line versus z. Moreover the shape of the blurring in the (x, z) plane appeared also very close to a Gaussian curve (Fig. 4A). Therefore, the simplest function was chosen that fit the three-dimensional behavior of the distortion,

$$I = \frac{a + b \cdot \exp^{-((x-c)^2/2\cdot d^2)}}{(z - e \cdot \exp^{-((x-c)^2/2\cdot d^2)})^2 + \left(\dfrac{f}{\exp^{-((x-c)^2/2\cdot g^2)}}\right)}, \quad [3]$$

for a magnetization localized at the position (e, c). The letters a to g were adjustable parameters. Even though the B_1 attenuation on the x-axis was expected to be Lorentzian (Fig. 2D), the experimental profile shown in Fig. 3D was better fitted to a Gaussian line. The Lorentzian dependence on the z axis is simply due to the $T_{1,2}$ exponential damping of the pseudoFIDs, where $T_{1,2} = 0.5 \times (1/T_1 + 1/T_2)$. Equation [3] is applicable to calculate distorsion matrices for any image dimensionality. In order to compensate the coil receptivity ($\alpha(z)$ in Eq. [1]) along the z-axis, the intensity of the calculated distorted images was linearly increased as a function of the z-position of the single-pixel object. The slope of the correction function was calculated from the experimental B_1 distribution. Once the distortion matrix was known, the simplest way to find $M_{i,j}$ from any distorted image $I_{k,l}$ was to calculate the inverse distortion matrix. Unfortunately, this procedure had to be ruled out because the result of the product (distortion matrix)$^{-1} \times I_{k,l}$, although compatible with the data from a mathematical point of view, was never physically realistic because of noise fitting. A preferred approach was to compare in an iterative way the product (distortion matrix $\times M_{i,j}$) to $I_{k,l}$. The starting image was made from $I_{k,l}$ taking into account the most highlighted pixels in each profile. Refining of $M_{i,j}$, was carried out using a χ^2 minimization test and was achieved in less than 30 iterations. All calculations, i.e., B_1 field simulations, curve fittings, and image reconstructions were carried out using Igor Pro (Wavemetrics, Lake Oswego, OR, USA).

Figure 4B shows the correction brought by the reconstruction protocol to the image depicted in Fig. 4A. Clearly the blurring disappeared and the position of the phantom appeared quite obviously. Correction of more complicated images was evaluated using other water phantoms. The drawback of such experiments is the B_0 homogeneity optimization, which became more difficult as the size of the phantoms increased. Linewidths could attain 100 Hz, which precluded a good resolution on the z axis, because T_2^* had a nonnegligible damping effect on the pseudoFIDs (*8, 15*). The T_2^* damping also reduced the signal-to-noise ratio. Nevertheless, it was possible to obtain artifacted images from two cylinders (along the y axis) similar to that presented in Fig. 4 (Fig. 5A) or from three vials along the z axis (Fig. 5C). Reconstructed magnetization maps are illustrated on Figs. 5B and 5D. Taking into account the poor B_0 homogeneity, the quality of such images may be taken as reasonable. Different objects made of phantoms of different size were also investigated in this way, and the results were in agreement with their real shape.

The image resolution depends on different parameters. The most important variable is the B_1 gradient intensity generated along the z-axis. The B_1 field simulation and measurement showed a linear evolution on 75% of the coil length (15 cm) at 4 cm depth. In order to be correctly separated on the profile, two small phantoms (1 cm diameter) had to be a distant 3 cm away. In the localization sequence, the radiofrequency pulse amplitude and duration determined the image field of view. Before measurements, it was necessary to calibrate precisely the RF pulse to achieve the minimal field of view for a specific object. The adjustment test was an image aliasing whenever the field of view was too small. The other resolution parameter is the sample size determined by the number of radiofrequency pulses. In order to maintain a sufficient signal-to-noise ratio, 128 data points have been selected. In the second direction

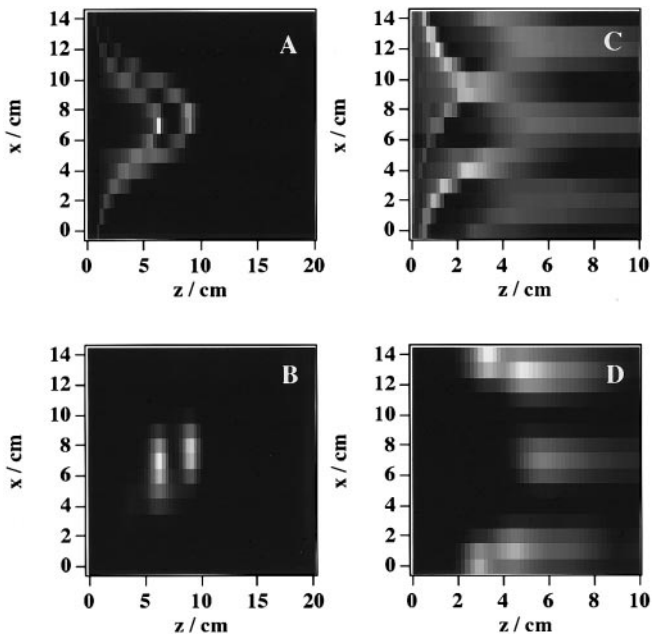

FIG. 5. Distorted images of two water cylinders (1 cm diameter, A) and of three 5-mL water vials (7 cm length, 1 cm diameter, C). Reconstructed images are displayed in (B) and (D). Experimental conditions: pulse length 800 μs, $G_1 = 23$ μT/m (A) or 46 μT/m (C), 128 RF pulses.

(x-axis), the number of profiles determined the image resolution. Moreover, it could be noticed that the method is not limited by the size of the object in the x-direction, in the area of B_0 homogeneity.

The method presented here shows some advantages. Indeed, since no B_0 gradient coils are necessary, a simplification and a cost reduction of the MRI system dedicated to B_1 imaging might be considered. The localization method can be easily used for medical applications in order to build a small and simple MRI instrument as easy to handle as an ultrasonic device. For low B_0 applications, in order to increase the signal-to-noise ratio, the present system could be combined with a prepolarization unit without risk of interaction between the B_0 gradient and the B_0 field during the switching phases (*16*). It could then be used for industrial applications as on-line product control (food-industry, chemistry, etc.) in open magnets. Among the limitations of the method was the absence of slice selection. All the presented results have been achieved on quasi-planar objects. Work is in progress to develop different strategies to solve this problem without using any other coil. Shaka and Freeman (*17*) have demonstrated the capability of spatial localization with the use of a composite pulse scheme for exciting an NMR response only when B_1 is near a nominal value B_1^0. Such a principle might be applied to improve the slice localization using adiabatic pulses (*18*).

ACKNOWLEDGMENT

We are grateful to Dr Lionel Canioni (CPMOH, University of Bordeaux 1) for his enlightened help in signal processing.

REFERENCES

1. D. I. Hoult, Rotating frame zeugmatography, *J. Magn. Reson.* **33,** 183–197 (1979).
2. D. Canet, RF field gradient experiments, *Prog. NMR Spectrosc.* **30,** 101 (1997).
3. A. A. Maudsley, Fourier imaging using RF phase encoding, *Magn. Reson. Med.* **3,** 768–777 (1986).
4. D. Canet, D. Boudot, A. Belmajdoub, A. Retournard, and J. Brondeau, Accurate spatial localization by a novel sequence using a RF field gradient and a DANTE-like pulse train, *J. Magn. Reson.* **79,** 168–175 (1988).
5. D. Boudot, D. Canet, J. Brondeau, and J. C. Boubel, DANTE-Z. A new approach for accurate frequency selectivity using hard pulses, *J. Magn. Reson.* **83,** 428–439 (1989).
6. P. Maffei, K. Elbayed, J. Brondeau, and D.Canet, Slice selection in NMR imaging by use of the B_1 gradient along the axial direction of a saddle-shaped coil, *J. Magn. Reson.* **95,** 382–386 (1991).
7. J. P. Boehmer, K. R. Metz, J. Mao, and R. Briggs, Spatial mapping of ^{23}Na NMR signals by two-dimensional rotating frame imaging, *Magn. Reson. Med.* **16,** 335–341 (1990).
8. P. Maffei, P. Mutzenhardt, A. Retournard, B. Diter, R. Raulet, J. Brondeau, and D. Canet, NMR Microscopy by RF field gradients, *J. Magn. Reson. A* **107,** 40–49 (1994).
9. G. S. Karczmar, D. B. Twieg, T. J. Lawry, G. B. Matsonand, and M. W. Weiner, Detection of motion using B_1 gradients, *Magn. Reson. Med.* **7,** 111–116 (1988).
10. D. Canet, B. Diter, A. Belmajdoub, J. Brondeau, J. C. Boubel, and K. Elbayed, Self-diffusion measurements using a radiofrequency field gradient, *J. Magn. Reson.* **81,** 1–12 (1989).
11. F. Humbert, B. Diter, and D. Canet, NMR microscopy by strong RF-field gradients with spatial resolution better than five micrometers, *J. Magn. Reson. A* **123,** 242–245 (1996).
12. F. Humbert, M. Valtier, A. Retournard, and D. Canet, Diffusion measurements using RF field gradient: Artifacts, remedies, practical hints, *J. Magn. Reson.* **134,** 245–254 (1998).
13. S. Akoka, F. Franconi, F. Seguin, and A. Le Pape, Radiofrequency map of an NMR coil by imaging, *Magn. Reson. Imaging* **11,** 437–441 (1993).
14. D. Boudot, D. Canet, and J. Brondeau, Spatial labelling by a radiofrequency field gradient. DANTE-Z profile, probed by one-dimensional nutation imaging, *J. Magn. Reson.* **87,** 385–394 (1990).
15. J. C. Sharp, R. W. Bowtell, and P. Mansfield, Elimination of susceptibility distortions and reduction of diffusion attenuation in NMR microscopy by line-narrowed 2DFT, *Magn. Reson. Med.* **29,** 407–411 (1993).
16. A. Macovsky and S. Conolly, Novel approaches to low-cost MRI, *Magn. Reson. Med.* **30,** 221–230 (1993).
17. A. J. Shaka and Ray Freeman, Spatial localisation in NMR, *Adv. Magn. Reson. Techniques Syst. High Mol. Complexity PBB* **2,** 1–19 (1986).
18. R. A. de Graaf, R. Nicolay, and M. Garwood, Single-shot, B_1-insensitive slice selection with a gradient-modulated adiabatic pulse, BISS-8, *Magn. Reson. Med.* **35,** 652–657 (1996).